Acta Materialia 211 (2021) 116879

Contents lists available at ScienceDirect

Acta Materialia

journal homepage: www.elsevier.com/locate/actamat

Full length article

Unveiling the mechanism of yttrium-related microstructure inhibiting or promoting high-temperature oxidation based on Ni-Al-Y alloys

Yun Wu[a,b], Yunting Li[c], Yuantao Xu[b,d], Maodong Kang[a,b,*], Jun Wang[a,b,*], Baode Sun[a,b]

[a] Shanghai Key Laboratory of Advanced High-temperature Materials and Precision Forming, Shanghai Jiao Tong University, Shanghai 200240, China
[b] School of Materials Science and Engineering, Shanghai Jiao Tong University, Shanghai 200240, China
[c] Instrumental Analysis Center, Shanghai Jiao Tong University, Shanghai 200240, China.
[d] Shanghai Key Laboratory of Materials Laser Processing and Modification, Shanghai Jiao Tong University, Shanghai 200240, China

ARTICLE INFO

Article history:
Received 25 November 2020
Revised 7 March 2021
Accepted 2 April 2021
Available online 8 April 2021

Keywords:
Nickel-based superalloy
Yttrium distribution
Oxidation
Oxide evolution
Thermodynamics

ABSTRACT

Yttrium is an attractive component for nickel base alloys to improve high-temperature oxidation resistance. However, the application suffers from microstructure related problem, due to less unconscious of Y-related oxidation behavior, especially interacting with other key components, such as aluminium. This study introduces the discovery of microstructure depended external and internal oxidation behaviors based on four simplified Ni-Al-Y alloys during isothermally exposing at 800°C/1000°C in air. Using multiscale microstructural characterizations and thermodynamic calculations, different oxidation layer thicknesses have been observed in the four alloys, especially varying with Y and Al concentrations. In the three high-Y-content alloys, Y-related microstructures are found to strongly drive the oxidation process. Original-Ni_5Y compound with strong tendency to precipitate secondary γ-Ni strip is favorable to the formation of inner oxidation layer containing mixed oxide particles, whereas original-γ-Ni phase drives the formation of outer scale of NiO. Dense and well-configured lamella-like phase boundaries (PBs) are beneficial to inhibiting the development of the inner layer, compared to coarse and irregular PBs. The resistance to inner oxidation of minor-Y-addition alloy has been significantly improved at 1000°C, benefiting from the mixed oxides along grain boundaries (GBs) and front of inner oxidation layers. From the thermodynamic basis, a type of modified diagram retrieved from ternary isothermal section is utilized to exhibit the oxide evolution, which is consistent with experimental results, especially for those complicated products.

1. Introduction

The development of high thrust aircraft engine and advanced ultra-supercritical coal-fired power plant is inseparable from the support of gas turbine and key components, *e.g.*, combustion chamber, turbine, and high-pressure compressor, as well as those corresponding pieces of turbomachinery, *e.g.*, rotors, blades, inner and outer cases, and discs [1-4]. High-performance materials, especially nickel-based superalloys featured by an excellent combination of high-temperature strength, toughness, ductility, and oxidation resistance, play a vital role in keeping these components reliable during service [5-7]. However, the long-term and complex high-temperature service environment still makes nickel-based superalloys face great challenges, one of which is oxidation resistance [8-10]. This life-limiting property drives the consumption of alloy components and the formation of outer and/or inner oxides, which consequently leads to the degradation of surface microstructure [6]. Typically, the formation of oxides depends strongly on the inward and outward diffusion of oxygen anions (O^{2-}) and metal cations, respectively, as well as the migration of electronics [11]. These diffusions and reactions make the chemical composition of alloy surface deviate from the substrate, thusly leading to undesirable microstructural problems, *e.g.*, element depletion zone, oxidation pits, and isolated oxide particles [9-11]. Apparently, these kinds of microstructural degradation destroy the continuity of the matrix and facilitate the formation of strain localization, which could predominantly affect the key properties of alloys, such as stress rupture [12], creep [13-15], and fatigue [15-17].

* Corresponding authors.
E-mail addresses: kangmd518@sjtu.edu.cn (M. Kang), junwang@sjtu.edu.cn (J. Wang).

https://doi.org/10.1016/j.actamat.2021.116879
1359-6454/

High-temperature oxidation behavior has been widely studied from the aspects of thermodynamics and kinetics [6,8,18-25]. The Gibbs free energy of formation (ΔG_f) of an oxide is usually used to understand the stability or oxygen affinity of a specific alloy component [6,8]. Sometimes it is necessary to explain the migration of anions, cations and electrons, which involves distinguishing the type of oxidation product (n-type or p-type semiconductors) [6,18,26]. Moreover, special attention should be paid to the alloy composition, considering its significant influence on formation of continuous or protective oxide scale. The introduction of reactive component (such as Y) has been proved to be effective in improving high-temperature oxidation resistance [27-32], due to the reported mechanisms, *e.g.*, reacting with sulphur [29], lower development of inner oxidation [30], and improving adhesion of protective oxide scale [31,32]. Previous study demonstrated that the oxygen activity at the scale/substrate interface of a Y-doping alloy (being Al_2O_3-scale former) is lower than that of Y-free alloy (Cr_2O_3-scale former), which indirectly proves that Y promotes the outward diffusion of Al and selective formation of Al_2O_3 scale [27]. However, due to the limited amount of Y, the exact theoretical and experimental basis concerning the effect of Y in nickel-based superalloys still remains inadequate, especially ignoring the existence of Y-related microstructures. The Ni-Y compounds have been well discussed in nickel-based bond coat material, *i.e.*, NiCoCrAlY [33-36], and proved to be favorable to the formation of (Y, Al)-rich oxides, *e.g.*, $YAlO_3$ (Y-Al perovskite, denoted as YAP) [35], $Y_4Al_2O_9$ (Y-Al monoclinic oxide, YAM) [36], and $Y_3Al_5O_{12}$ (Y-Al garnet, YAG) [37]. Affected by these oxides, the growth of Al_2O_3 scale can be inhibited or promoted, depending on the size of (Y, Al)-rich pegs within Al_2O_3 scale [24,35]. However, these excellent findings have not yet been applied to explaining the oxidation behavior of Y-containing nickel-based superalloy. Apart from this, the evolution of Y-related microstructures during oxidation has not yet been well explained. Except for these, the protective effect of other component (providing necessary ability to promote the external growth of Al_2O_3) or the classical oxidation theory [38-40], should also be considered, especially under the influence of reactive element Y.

In the present study, isothermal oxidation in air at 800°C/1000°C has been conducted to investigate the oxidation mechanisms and microstructural characterizations, coupled with thermodynamic calculations, of four types of Ni-Al-Y alloys. Special attention has been put on the effect of (Ni, Y)-rich compound, *i.e.*, Ni_5Y, on the growth of both outer and inner oxides. The effect of Y concentration on scale thickness or oxidation rate has been revealed. It is interestingly found that excessive Y does not necessarily mean the increase of oxidation rate. Detailed mechanism needs to be discussed in combination with Y-related microstructural features. We therefore show the importance of micro-morphology in the oxidation process: coarse Ni_5Y phase (proeutectic phase) does not improve oxidation resistance, while fine Ni_5Y compound (nanoscale eutectic lamellae) do so apparently. By simplifying the alloy components, we have successfully revealed the formation process of YAM and κ-Al_2O_3 within original-Ni_5Y phase at 800°C, based on the precipitation-related transport mechanism concerning secondary γ-Ni strips during isothermal exposure. The classical criteria for the formation of Al_2O_3 was also used to explain the significantly improved resistance to inner oxidation of 22Al10Y at 800°C, and minor-Y-addition 10Al0.5Y at 1000°C. Further, a thermodynamic-based method coupled with post-processing for predicting complex oxidation products has been utilized to exhibit the oxide evolution. The predicted products are in excellent agreement with experimental results, especially for the prediction of YAM. The findings in the present investigation is effective to predicting the steady-state oxidation products and to designing multi-component and anti-oxidation nickel-based alloy or bond coat material containing Al and Y.

2. Materials and methods

2.1. Materials preparation and isothermal oxidation

Various Ni-Al-Y ingots were synthesized using vacuum arc-melting of high purity (>99.99 wt.%) elemental constituents in a titanium-getter argon atmosphere. A type of ingot with eutectic microstructure, namely Ni-22.34Al-10.13Y (at.%, hereinafter simplified as 22Al10Y), was pre-determined using inductively coupled plasma optical emission spectroscopy (ICP-OES, Thermo Scientific iCAP7600) and field-emission scanning electron microscope (SEM, TESCAN MIRA3). The other two types of ingots with hypoeutectic (Ni-10.25Al-3.38Y or 10Al3Y) and hypereutectic (Ni-10.36Al-10.27Y or 10Al10Y) microstructures, respectively, were later acquired by adjusting chemical compositions according to 22Al10Y and assessed liquidus projection [41]. In addition, the fourth Ni-Al-Y alloy with minor Y content was also considered, *i.e.*, Ni-10.13Al-0.52Y (10Al0.5Y). The detected chemical compositions of the four alloys are listed in Table 1.

Bulk samples with a uniform dimension of 10.5 × 10.5 × 2.5 mm were machined from the as-melted ingots. To ensure uniform oxidation, all surfaces of the bulk samples were carefully ground down to a P3000 SiC grit paper, followed by ultrasonic cleaning in acetone. Isothermal oxidation tests were carried out at 800°C and 1000°C respectively in a chamber furnace under laboratory air for a maximum duration of 200 h. Particularly, each sample was hung in an alumina crucible with a platinum wire to expose all surfaces. After a required exposure time, samples were air-cooled outside the furnace and subsequently preserved in a laboratory oven at 70°C before further testing.

2.2. Microstructural and elemental characterization

To examine original microstructures, as-cast samples were machined from the prepared ingots. These samples were mechanically ground down to a P3000 SiC grit paper, polished down to 1 μm diamond solution, and finally vibration-polished in 50 nm silica suspension for 2 h. After these, the phases within as-cast microstructures were examined by X-ray diffraction (XRD) measurements using Bruker D8 ADVANCE X-ray diffractometer, and by electron backscatter diffraction (EBSD, Oxford Instruments NordlysMax3), equipped in the SEM, respectively. The EBSD maps were acquired under a step size of 50~100 nm with an electron beam accelerating voltage of 30 kV and current of tens of nA. Post-EBSD data processing was mainly realized by AZtecCrystal software (version 1.1), and also referred to the open source toolbox MTEX (version 5.4.0) based on MATLAB (version 2020a) [42], and ATEX software (version 2.16) [43]. The samples were chemically etched in a solution of 5 g $CuCl_2$, 100 ml HCl, and 100 ml absolute alcohol, for 5~10 s and finally analyzed using the SEM and energy dispersive X-ray spectroscopy (EDS, Oxford Instruments X-Max^N).

After oxidation, species within oxide scales were detected by XRD. To understand the morphologies and compositions of oxidation products, oxidized surfaces and cross-sections of the samples were preliminarily analyzed using SEM and EDS. For transmission electron microscopy (TEM) analysis, thin foils were extracted from specific locations of the cross-sectional samples using focused ion beam (FIB) lift-out methods in a TESCAN GAIA3 ultra-high-resolution SEM-FIB system equipped with a Ga+ focused ion beam accelerating voltage of up to 30 kV and current of 1 pA~50 nA. At the final stage of the sectioning, the foils with a thickness of ~100 nm were carefully cleaned at decreasing high voltages and currents ranging from 5 kV, 100 pA to 5 kV, 40 pA. TEM and scanning transmission electron microscopy (STEM) analyses on oxidized microstructures were conducted on Schottky field-emission FEI Talos F200X G2 (20-200 kV) equipped with Super-X four SDD enhanced

Table 1
Chemical compositions, phases, and corresponding elemental constitutions of the investigated alloys.

Alloy notation	As-cast composition (at.%)			Microstructure description	Component in a phase (at.%)				
					NiAl/γ-Ni		Ni_5Y		
	Al	Y	Ni		Ni	Al	Ni	Y	Al
22Al10Y	22.34	10.13	bal.	Eutectic (NiAl+Ni_5Y)	53.65	46.35	70.12	15.24	14.64
10Al3Y	10.25	3.38	bal.	Proeutectic γ-Ni + Eutectic (γ-Ni+Ni_5Y)	85.41	14.59	82.46	12.93	4.61
10Al10Y	10.36	10.27	bal.	Proeutectic Ni_5Y + Eutectic (γ-Ni+Ni_5Y)	81.06	18.94	79.24	14.36	6.40
10Al0.5Y	10.13	0.52	bal.	γ-Ni (matrix)+ (γ-Ni+Ni_5Y)	88.29	11.71	-	-	-

EDS detectors. High angle annular dark field (HAADF) STEM imaging was performed using a convergence angle of 10.5 mrad, an inner angle of 58 mrad, and an outer angle of 200 mrad. STEM-EDS spectral imaging was realized using a probe current of 800 pA. The FIB foils were also used for Transmission Kikuchi diffraction (TKD) analyses by using the same equipment as the aforementioned EBSD experiment (with a step size of ~30 nm).

2.3. Calculation of Gibbs free energy of formation

Instead of simply adopting standard Gibbs free energy of formation (ΔG_f^0) of potential oxides [40,44], the present investigation calculated actual value of ΔG_f by considering local element concentration within specific phases [6,8]:

$$\Delta G_f = \Delta G_f^0 + RT\ln\left(\frac{a_{M_xO_y}^{2/y}}{a_M^{2x/y}\cdot p_{O_2}}\right) \quad (1)$$

where T is absolute temperature, and R is the gas constant. M and M_xO_y represent metal reactant and oxidation product, respectively. The x and y containing exponents are the stoichiometric coefficients of chemical equation relating to the product M_xO_y. Therefore, a is the corresponding activity. Generally, $a_{M_xO_y}$ is taken to be unity, and a_M is taken based on the local concentration and finally calculated using Thermo-Calc software. The partial pressure of oxygen (p_{O_2}), is determined based on the laboratory condition, *i.e.*, 0.2 atm in 1 atm of air. Approximately, ΔG_f^0 can be calculated according to:

$$\Delta G_f^0 = \Delta H_{298}^0 - T\Delta S_{298}^0 \quad (2)$$

$$\Delta H_{298}^0 = \sum_i p_i \Delta H_{i,298}^0 - \sum_j r_j \Delta H_{j,298}^0 \quad (3)$$

$$\Delta S_{298}^0 = \sum_i p_i S_{i,298}^0 - \sum_j r_j S_{j,298}^0 \quad (4)$$

where ΔH_{298}^0 and ΔS_{298}^0 are the standard enthalpy and entropy of formation of the oxidation products at 298 K, respectively. $\Delta H_{i\ or\ j,298}^0$ and $\Delta S_{i\ or\ j,298}^0$ are the enthalpy and entropy of formation of the substance from the stable states of the elements at 298 K, respectively. i and j respectively describe the situation of reactants and products in the oxidation reaction. Correspondingly, r_j and p_i are the coefficients of reactants and products in the oxidation reaction, respectively. Generally, only two reactants and one oxidation product are considered in this study while calculating ΔG_f^0 and ΔG_f. Data corresponding to $\Delta H_{i\ or\ j,298}^0$ and $\Delta S_{i\ or\ j,298}^0$ of a specific substance can be found elsewhere [45,46]. The complete derivation process concerning ΔG_f^0 can refer to the relevant literature [44-47].

2.4. Thermo-Calc calculation

The activity of a specific component, *i.e.*, a_M, was calculated using Thermo-Calc software and TCNI8 database (hereinafter TC) [48,49] realized by PROPERTY-DIAGRAM module and the chemical concentration in a local phase. The calculated activity would be later used in calculating ΔG_f. Further, the ternary isothermal sections and corresponding modified diagrams were also calculated using TC, realized by Console mode and TERNARY_DIAGRAM module. The re-setting of reference state was realized by the command SET_REFERENCE_STATE in POLY_3 module. The diffusion coefficient of Al in γ-Ni matrix at a specific temperature was also calculated using TC, supported by DICTRA module, and thermodynamic database (TCNI8) and kinetic database (MOBNI4).

3. Results

3.1. Characterization of as-melted microstructures

Four Ni-Al-Y alloys are considered, *i.e.*, eutectic 22Al10Y, hypoeutectic 10Al3Y, hypereutectic 10Al10Y, and minor-Y-doping 10Al0.5Y. A summary of the mentioned microstructures and corresponding chemical compositions is listed in Table 1. SEM, EBSD, and XRD were performed to analyze the as-melted microstructures of the four alloys. The results reveal that 22Al10Y typically possesses lamella-like eutectic structure, composed of NiAl and Ni_5Y (Fig. 1a and Supplementary martials Fig. S1a). 10Al3Y possesses γ-Ni as proeutectic phase, and (γ-Ni+Ni_5Y) as eutectic structure (Fig. 1b and Fig. S1b). 10Al10Y possesses Ni_5Y as proeutectic phase, and (γ-Ni+Ni_5Y) as eutectic structure (Fig. 1c and Fig. S1c). Finally, 10Al0.5Y possesses γ-Ni as matrix and minor (γ-Ni+Ni_5Y) locating mainly in GBs (Fig. 1d and Fig. S1d). According to these results, Al has obvious solubility in Ni_5Y phase, which is in accordance with our thermodynamic calculations using TC [48,49], as shown in Fig. S2. It is critical to emphasize the solubility of Al in Ni_5Y, due to the calculation of actual ΔG_f later need the support of chemical concentration of specific component. In contrast, there is almost no solubility of Y in Ni. Therefore, the negligible Y content in γ-Ni is set to zero in the following thermodynamic calculations.

3.2. Oxidation products

After isothermal exposure at 800°C for 1~200 h, the morphologies and species of oxides on the sample surface were examined by XRD, SEM, and EDS (Fig. 2 and 3, Fig. S3 and S4). The XRD patterns indicate that various products present after one-hour exposure, *e.g.*, NiO, $NiAl_2O_4$, YAM, and YAP. With the increase of exposure time (up to 200 h), NiO and YAM still exist, while $NiAl_2O_4$ and YAP almost disappear (Fig. 2a). The surface morphologies of oxidation products evolve from fine oxide particles to larger and denser

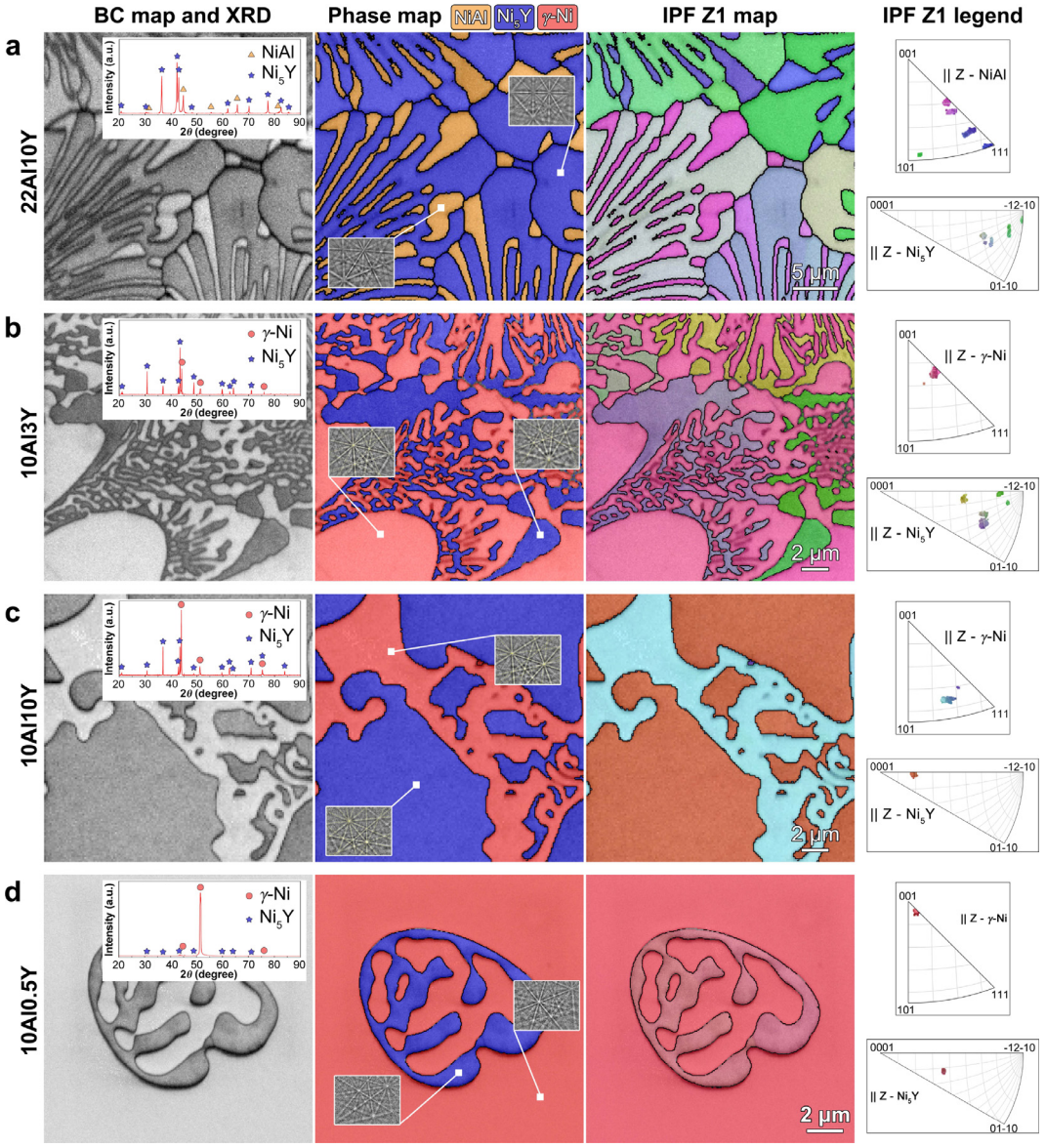

Fig. 1. EBSD and XRD analyses concerning phase characterization of the as-cast Ni-Al-Y alloys: (a)-(d) EBSD band contrast (BC) maps with inserted XRD patterns, phase maps with inserted Kikuchi patterns, inverse pole figures (IPF) along Z1 axis, and corresponding legends, of samples 22Al10Y, 10Al3Y, 10Al10Y, and 10Al0.5Y, respectively.

particles, as revealed in Fig. 2b. By combining the results of XRD and SEM, the presented surface oxide particles can be inferred to be NiO, which will be further determined by SEM-EDS and TEM studies in the following sections.

Fig. 3 shows the cross-sectional SEM images and elemental map of three 200-hour-exposed samples, indicating the strong dependence of oxidation behavior on original microstructure, *e.g.*, 22Al10Y exhibits lamella-like inner oxide layer, and 10Al3Y and 10Al10Y exhibit ones based on primary and eutectic phases. The post-oxidation microstructures of all the three alloys show similar continuous outer layer (probably NiO) but distinguished in thickness (Fig. 3 and Fig. S3). According to these observations, Y-rich and Al-rich or (Y, Al)-rich oxides are concentrated in the inner layer, indicating very first formation of these oxides due to the fast inward-flux of O^{2-} and high activity of Y and Al [24,50-52]. Particularly, some continuous dark-contrast oxides (rich in Al and O) present along the PBs between primary and eutectic phases in 10Al3Y and 10Al10Y.

For the case of 10Al0.5Y, the observed inner layer structure is quite different from the above three alloys. Without massive Y-related microstructure, 10Al0.5Y exhibits obvious characteristics of γ-Ni oxidation, *i.e.*, granular and rod-like oxides (Fig. S4), controlled by oxygen diffusion. Particularly, the front of inner oxide propulsion was occupied by Al-rich oxides.

The layer structures of 22Al10Y, 10Al3Y, and 10Al10Y after exposure at 1000°C for 200 h are similar to that of 800°C, except for the increased layer thickness (Fig. S5). As to the minor-Y-addition ones, 10Al0.5Y, its oxidation layer exhibits obvious changes after exposure at 1000°C. At 1000°C, the inner layer thickness decreased significantly, compared to that of 800°C (Fig. S4 and S6), indicating a better resistance to inner oxidation. The Al-rich oxides at the front of inner layer at 1000°C massively grew and became thicker and more continuous than that of 800°C. These changes found in the 10Al0.5Y alloy demonstrate that the potential oxidation behavior has obviously changed.

3.3. Oxidation kinetics

According to Fig. 3 and S4, the total oxide layer thickness of the three samples after oxidation is quite different. Further statis-

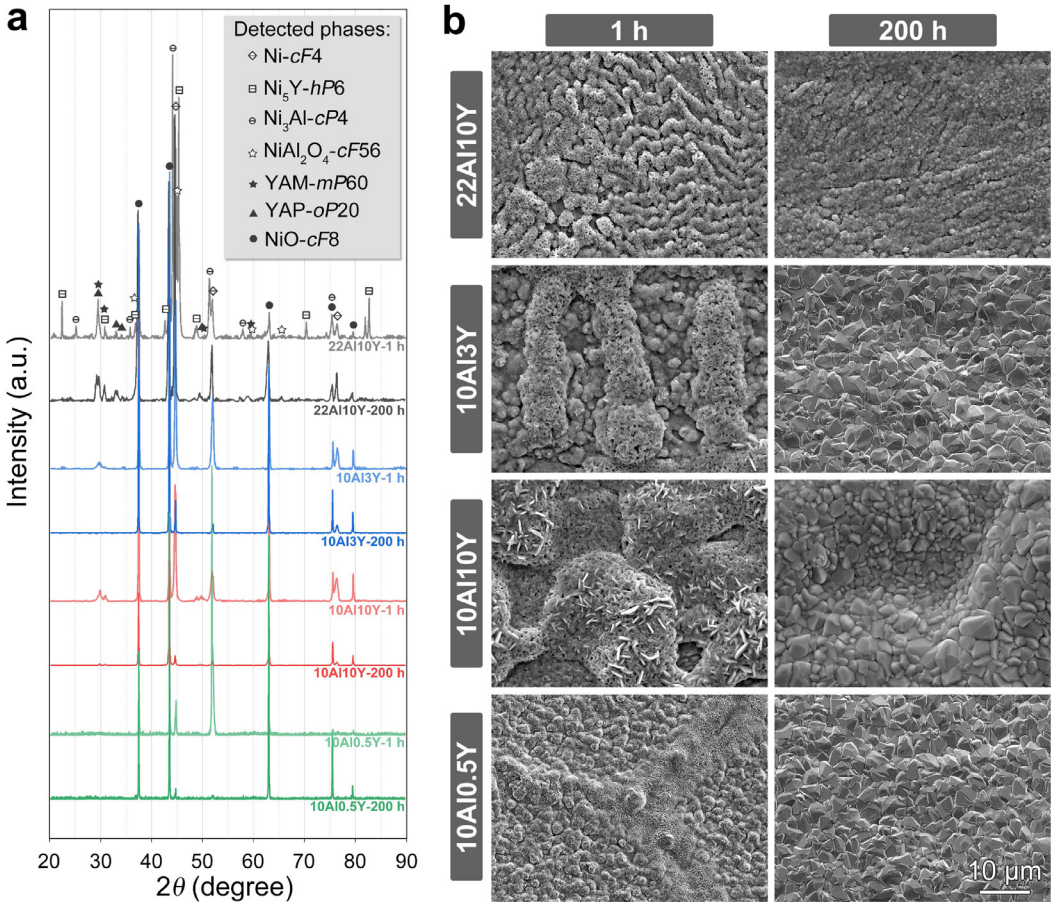

Fig. 2. XRD and SEM analyses of the 800°C-oxidized Ni-Al-Y alloys: (a) XRD patterns of the one-hour and 200-hour oxidized surfaces. (b) SEM secondary electron (SE) images showing the morphologies of oxidation products of the four Ni-Al-Y alloys after oxidized for 1 h and 200 h.

tical results concerning total thickness of oxide layer is exhibited in Fig. 4. It indicates 10Al10Y has the thickest oxide layer at all experimental periods, followed successively by 10Al0.5Y, 10Al3Y, and 22Al10Y at 800°C, and 22Al10Y, 10Al3Y, and 10Al0.5Y at 1000°C. Although the power exponents of these curves deviate from the exponent of classical parabolic law, the growth kinetics of oxide layer can be described by power law. In the early stage of oxidation, O^{2-} rapidly enter the subsurface of the alloys to react with the high-activity alloy components, resulting in the rapid increase of scale thickness (Fig. 4) and the formation of inner oxides (Fig. 5). With the increase of scale thickness, the metal activities near scale/alloy interface gradually decrease (finally approaching the equilibrium value of oxidation reactions), which means that the metal activity gradients in the scale gradually decrease, resulting in the decrease of ion flux and reaction rate (Fig. 4) [40].

The most noticeable changes of oxidation kinetics are the two alloys, 22Al10Y and 10Al0.5Y, which respectively becomes the minimum oxide thickness at 800°C and 1000°C (Fig. 4). The potential mechanisms corresponding to these changes will be analyzed and discussed in detail in the following sections after more detailed characterization.

3.4. Oxide evolution and thermodynamic determination at 800°C

Aforementioned results have partly explained the formation of oxidation products. In this section, TEM study, based on FIB foils, and thermodynamic calculations are performed to further clarify the exact species of oxides, aiming to propose a general method for predicting the oxide evolution. Fig. 6a shows the HAADF-STEM image and STEM-EDS mapping result, indicating consistent layer structure and oxide distribution in 22Al10Y after one-hour exposure at 800°C with above analyses. It is confirmed that the outermost oxide scale is NiO (Fig. 6b). Due to the depletion of Al and O in original-NiAl region (Fig. 6a), it could reasonably infer that with the increase of exposure time, Ni^{+} in the inner layer reacts with O^{2-}, resulting in the thickening of NiO scale externally. In the inner layer, the original-Ni_5Y region evolves into mixed phases containing YAM (grey contrast) and κ-Al_2O_3 (dark contrast) oxides, while Ni almost exists alone (Fig. 6c). κ-Al_2O_3 is a metastable alumina with an orthorhombic structure and featured by Al vacancies possibly not forming a hexagonal network or independent Al^{3+} occupying a tetrahedral position, differing from that of stable α-Al_2O_3 with a trigonal structure [53-57].

The oxidation products after exposure at 800°C for 200 h were analyzed in detail by using the inner layer FIB foil of 10Al10Y, considering the coarsen morphology of primary Ni_5Y and eutectic phases facilitating micro-scale observations. Fig. 7a shows that almost only Ni is left in the original-γ-Ni region belonging to eutectic microstructure, and O is not obviously enriched in same region, which means that γ-Ni suffered lightly oxidation and transferred into Ni-O interdiffusion zone, differing from outer NiO scale. The obvious change is that Al in γ-Ni almost diffused to the corresponding PBs, *e.g.*, Al and O are enriched at the interface, which is consistent with above descriptions. In contrast, the original-Ni_5Y region belonging to eutectic microstructure suffered relatively server oxidation, as the observed YAM and κ-Al_2O_3 (Fig. 7b). The extensively presenting YAM in both one-hour and 200-hour oxidation samples indicates that the high-activity Y and Al are indeed

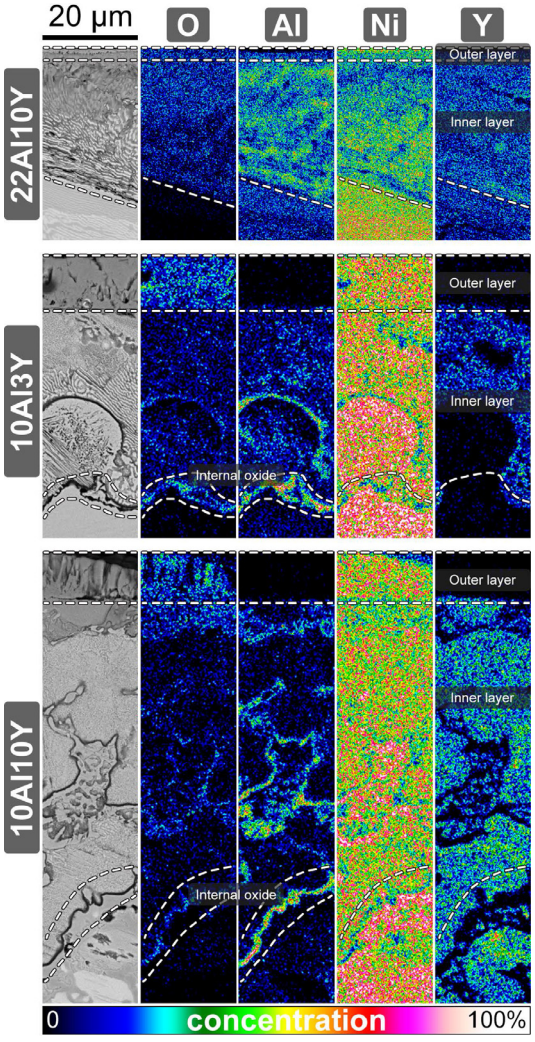

Fig. 3. Cross-sectional SEM backscattered electron (BSE) images and corresponding EDS mapping results showing the structures and elemental distributions of oxidation layers of the three high-Y-addition Ni-Al-Y alloys after 800°C-oxidized for 200 h.

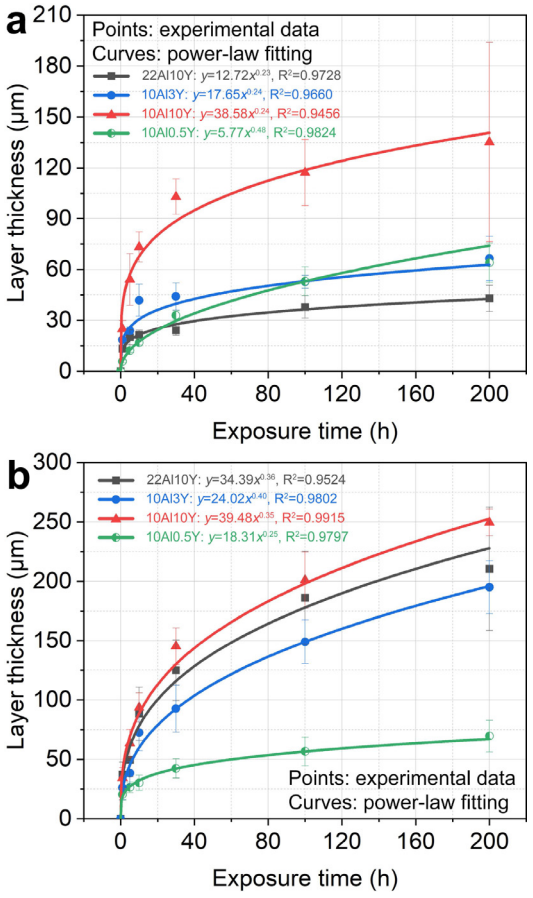

Fig. 4. Dependence of the oxidation layer thickness on the exposure time and corresponding fitting curves at 800°C (a) and 1000°C (b) showing the good consistent with power-law type equation.

reactive with O in the inner layer. Considering the existence of YAP (Fig. 2a), the whole reaction can be reasonably summarized as following:

$$Al2O3 + Y2O3 = 2YAlO3 \quad (5)$$

$$Al2O3 + 4Y2O3 + 4YAlO3 = 3Y4Al2O9 \quad (6)$$

Therefore, the inner layer corresponding to original-primary-Ni_5Y region is almost composed of YAM, κ-Al_2O_3 and non-oxidized γ-Ni. In addition, the PBs of both samples are almost occupied by Al rich oxides, which are partly composed of α-Al_2O_3 (Fig. S7).

Here we attempt to thoroughly understand the species within the oxide layers when the oxidation process become stable or local reactions reach equilibrium. This means equilibrium diagram, *e.g.*, isothermal section of ternary system under particular temperature, maybe useful in analyzing the species-related issue. Thus, three isothermal sections at 800°C, *i.e.*, Ni-Al-O, Al-Y-O, and Ni-Y-O, are calculated using TC (Fig. S8). Nevertheless, the accurate chemical composition in local area during oxidation remains unknown, which makes it difficult to link the actual oxides with the stable phases exhibited in the isothermal sections. To this end, a type of modified diagram is considered here, *i.e.*, replacing oxygen concentration with derived p_{O_2}, and retrieving the data corresponding to metal-component concentration verse p_{O_2} with resetting the reference state to O in gas phase (Fig. 8 and S9). The colored solid line indicates the solubility of the element indicated by y-axis in a phase (depending on p_{O_2}), and can also be regarded as the monophasic line. The area between two monophasic lines represents two-phase region.

Using the phase composition (Table 1) and some appropriate assumptions, the evolution of oxidation products or the final stable products can be inferred. The assumptions involve: i) Initial p_{O_2} is set to 0.2 atm (from 1 atm of air); ii) the equilibrium p_{O_2} of early reaction is iterated to later reactions; and iii) the evolution of oxidation products tend to change firstly along tie lines (perpendicular to two monophasic lines) or monophasic line. As to the formation of outer oxides NiO, Al concentration in initial NiAl phase of 22Al10Y is used, inferring the corresponding phases, *i.e.*, $NiAl_2O_4$+NiO (Fig. 8a). Apparently, either the formation of $NiAl_2O_4$ (common transient oxide) externally or Al-rich oxides internally leads to the decrease of Al concentration, which causes downward evolution of oxides, and finally reach and along NiO monophasic line, *i.e.*, forming stable NiO (Fig. 8a). Similarly, these analyses can be performed for the γ-Ni phase region in 10Al3Y, 10Al10Y, and 10Al0.5Y (Fig. 8a). Another situation, when local Al concentration stays supersaturation, the evolution path of products will deviate from the vertical tie lines, as the curved dot lines in Fig. 8a. Similarly, in Ni_5Y phase region, Y^{3+} reacts with O^{2-}, resulting in the decrease of Y concentration and facilitating the formation of NiO (Fig. S9).

As to the formation of inner YAM, κ-Al_2O_3, and α-Al_2O_3, Al concentration in initial Ni_5Y and p_{O_2} (0.2 atm) is used. Note that Ni

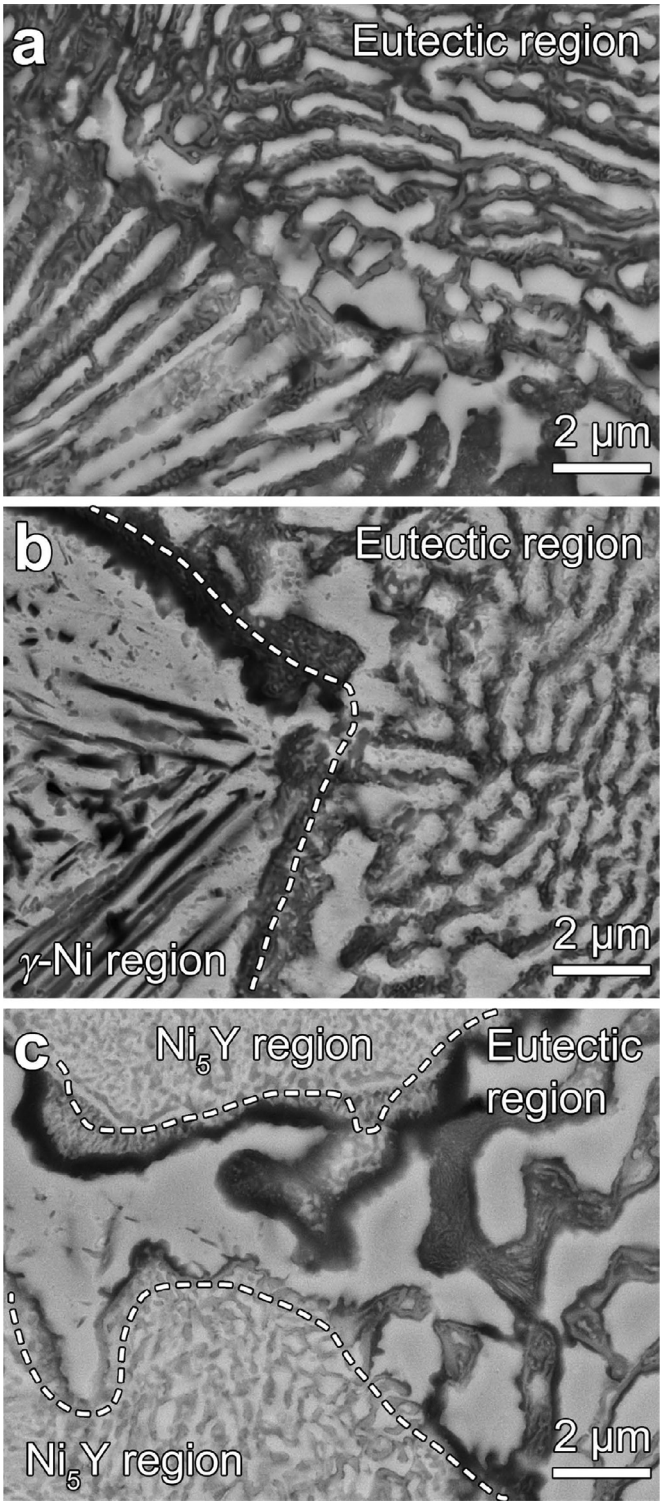

Fig. 5. (a)-(c) SEM-BSE images showing the microstructure-depended oxidation morphologies within inner layer after 200-hour exposure at 800°C of samples 22Al10Y, 10Al3Y, and 10Al10Y, respectively.

becomes very inactive while the existence of Al and Y. This means that considering only Al-Y-O system and modifying Al concentration (by excluding Ni) in local area is reasonable after initial oxidation (Fig. 8b). Due to the rapid reaction, the evolution path of oxidation products directly changes from the initial point to the new concentration. Therefore, for 22Al10Y, initial products locate in YAP+YAM. With the formation of Al-rich oxide, the oxidation products in 22Al10Y evolve downward with the oxidation process, *i.e.*, regressing to the monophasic line of YAM. Similarly, the evolution of oxidation products in 10Al3Y and 10Al10Y can also be deduced. It should be noted that the Al concentrations in 10Al3Y and 10Al10Y are below the YAM monophasic line (as highlighted by circle in Fig. 8b) when Ni is excluded. It is impossible for the oxidation products to evolve downward to generate more liquid ions (ION_LIQ), so the products would be as close as possible to the nearest stable phase, namely YAM. A similar analysis was not undergoing in 10Al0.5Y, because of the limited Ni_5Y fraction.

3.5. Oxide evolution and thermodynamic determination at 1000°C

The aforementioned SEM and kinetics results have demonstrated the main difference between the case of 1000°C and 800°C lies in the alloy 10Al0.5Y and 22Al10Y. Here we checked the microstructure evolution of 10Al0.5Y after exposure at 1000°C for 200 h in detail. The HAADF-STEM image and corresponding STEM-EDS mapping results of inner layer demonstrate that Al-rich and Y-rich oxides possess a large area at the GBs (Fig. 9a). The SAED pattern of the Al-rich area demonstrates that two Al-O oxides present, *i.e.*, α-Al_2O_3 and κ-Al_2O_3 (Fig. 9b). According to the BF-STEM image, there are two sizes of grains in the Al-O oxide area along GBs. Moreover, the TKD analysis (Fig. S10) has additionally explained that the coarse grains are mainly α-Al_2O_3. Around the GBs, NiO and YAP were determined (Fig. 9b). The oxide evolution at 1000°C has also been analyzed by the thermodynamic method (Fig. S11). Again, the predicted oxides evolution paths along the phase lines are in good agreement with the experimental results, *e.g.*, the outer NiO layer and the inner YAP oxides.

4. Discussion

4.1. Oxygen affinity

In order to well understand the oxidation process of Ni, Al and Y, it is necessary to evaluate the stability or formation ability of their respective oxides, which is usually realized by comparing ΔG_f^0 or using Ellingham Diagrams [6,40,44]. However, for the actual situation, it is necessary to consider the chemical composition in local area, due to the existence of micro-segregation or various phases. Moreover, the actual value of p_{O_2} should be considered to calculate actual ΔG_f or modified Ellingham Diagrams [6]. By using the acquired chemical composition of various phases Table 1) and the method described in Section 2.3 (Eq. (1)-((4)), the present study calculated the ΔG_f of three stable oxides, *i.e.*, Y_2O_3, Al_2O_3, and NiO (Table 2 and 3, and Fig. S12). These results indicate that the formation ability are ordered in: Y_2O_3>Al_2O_3>NiO, or the oxygen affinity: Y>Al>Ni, which explains again the preferentially formation of the Y-rich and Al-rich or (Y, Al)-rich oxides beneath the alloy surface [40,50]. Note that, except for the continuous Al-O films along PBs, there is little sign of continuous inner oxide layer in the case of 800°C, but significantly found in the case of 10Al0.5Y after 1000°C exposure (Fig. S6). Owing to the limited area of Y-related phases in 10Al0.5Y, the growing of internal continuous Al-rich oxides becomes gradually at 800°C, and extensively at 1000°C (Fig. S4 and S6).

4.2. Oxidation mechanism corresponding to Y-related microstructure

The observed oxides and their formation area are partly consistent with the thermodynamic theory (ΔG_f, Fig. S12) as well as transport feature in bulk and PBs regions [11]. However, further explanation, especially concerning the formation of YAM, has not yet been involved. As described above, the three high-Y-content alloys are similar in oxidation layer structure after isothermal oxi-

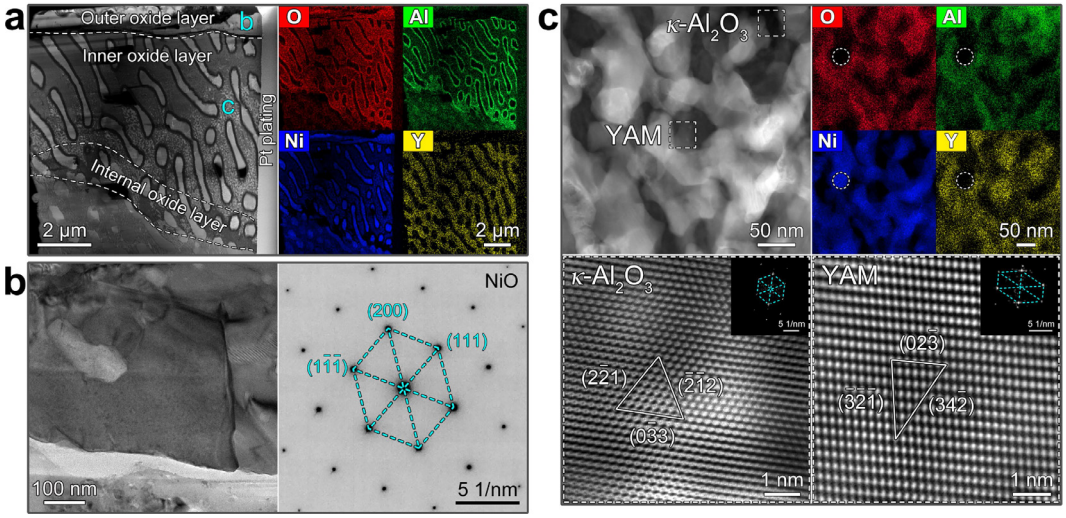

Fig. 6. Elemental distribution and oxidation species determinations via TEM performed on the 800°C-oxidized 22Al10Y: (a) HAADF-STEM image and corresponding drift-corrected STEM-EDS mapping result showing the layer structure and elemental distribution from outer to inner after one-hour exposure. (b) TEM bright-field (BF) image and corresponding selected area electron diffraction (SAED) pattern of the region indicated in (a) indicating the outer existence of NiO. (c) Enlarged HAADF-STEM image of the region indicated in (a) and STEM-EDS mapping result, and inverse fast Fourier transform (IFFT) images of the framed regions showing the elemental distribution and oxidation products.

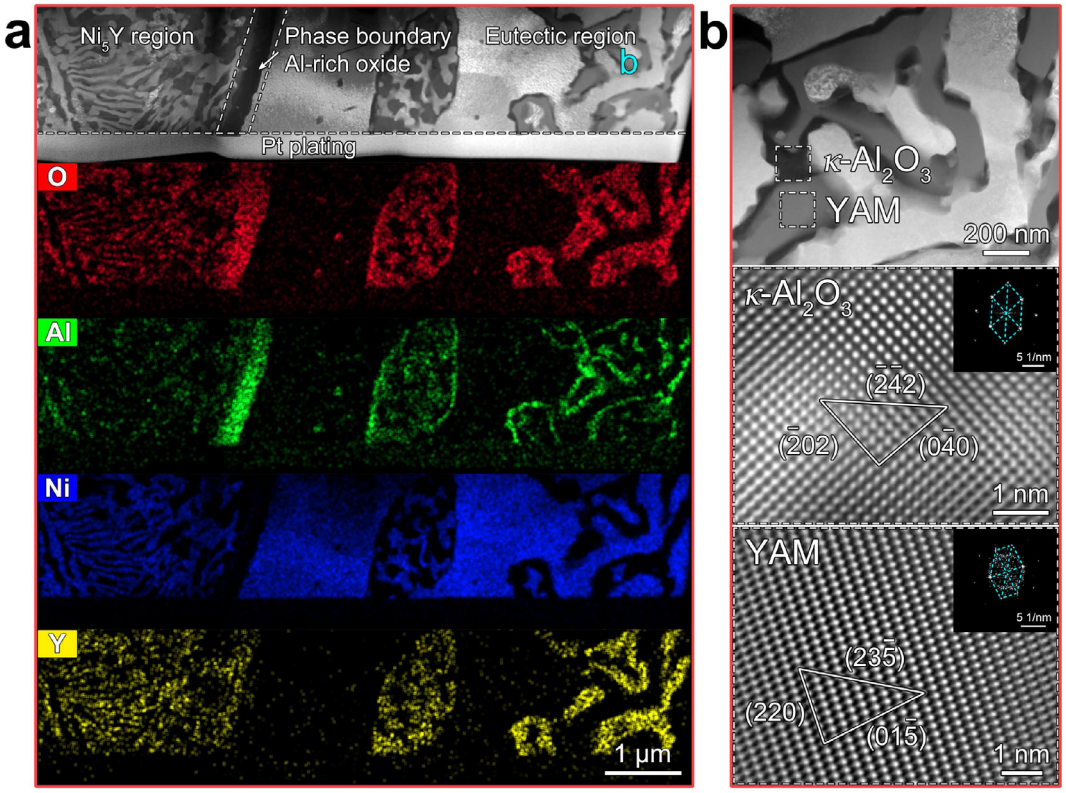

Fig. 7. Elemental distribution and oxidation species determinations via TEM performed on the 800°C-oxidized 10Al10Y: (a) HAADF-STEM image and corresponding drift-corrected STEM-EDS mapping result showing the inner layer structure and elemental distribution after 200-hour exposure. (b) Enlarged HAADF-STEM image of the region indicated in (a) and IFFT images of the framed regions showing the oxidation products.

Table 2
Relevant thermodynamic results (1073 K) calculated according to the phase constitution exhibited in Table 1.

Alloy notation	Situation in NiAl/γ-Ni at 1073 K				Situation in Ni_5Y at 1073 K					
	AC(Ni)	ΔG_f(NiO) (kJ/mol)	AC(Al)	$\Delta G_f(Al_2O_3)$ (kJ/mol)	AC(Ni)	ΔG_f(NiO) (kJ/mol)	AC(Al)	$\Delta G_f(Al_2O_3)$ (kJ/mol)	AC(Y)	$\Delta G_f(Y_2O_3)$ (kJ/mol)
22Al10Y	2.55×10^{-4}	-116.80	2.00×10^{-7}	-694.94	5.98×10^{-4}	-132.00	4.55×10^{-8}	-677.35	2.82×10^{-8}	-836.52
10Al3Y	2.70×10^{-3}	-158.91	1.07×10^{-9}	-632.70	1.45×10^{-3}	-147.80	6.75×10^{-11}	-599.87	2.34×10^{-8}	-834.27
10Al10Y	2.70×10^{-3}	-158.91	1.07×10^{-9}	-632.70	1.41×10^{-3}	-147.35	2.11×10^{-10}	-613.45	1.71×10^{-8}	-830.54
10Al0.5Y	2.91×10^{-3}	-160.23	6.33×10^{-10}	-626.51	-	-	-	-	-	-

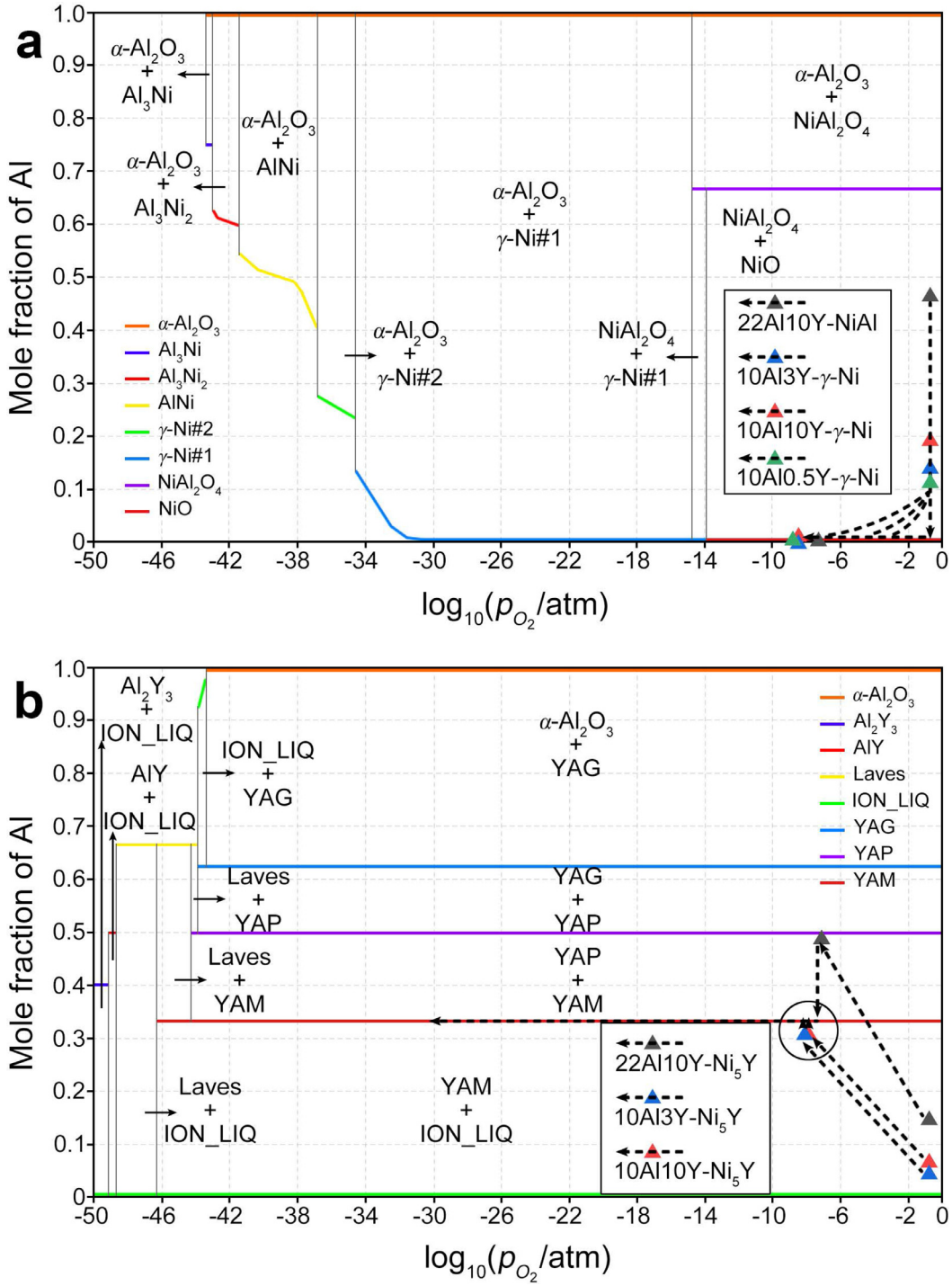

Fig. 8. (a), (b) Modified diagrams with re-setting reference state retrieved from ternary isothermal sections (800°C) of Ni-Al-O and Al-Y-O systems, respectively, showing the dependence of mole fraction of Al on partial pressure of oxygen.

Table 3
Relevant thermodynamic results (1273 K) calculated according to the phase constitution exhibited in Table 1.

Alloy notation	Situation in NiAl/γ-Ni at 1273 K				Situation in Ni_5Y at 1273 K					
	AC(Ni)	ΔG_f(NiO) (kJ/mol)	AC(Al)	ΔG_f(Al_2O_3) (kJ/mol)	AC(Ni)	ΔG_f(NiO) (kJ/mol)	AC(Al)	ΔG_f(Al_2O_3) (kJ/mol)	AC(Y)	ΔG_f(Y_2O_3) (kJ/mol)
22Al10Y	2.03×10^{-4}	-44.08	1.04×10^{-6}	-639.58	5.21×10^{-4}	-63.99	1.44×10^{-7}	-611.66	7.33×10^{-8}	-769.15
10Al3Y	1.64×10^{-3}	-88.31	1.28×10^{-8}	-577.54	1.13×10^{-3}	-80.35	4.67×10^{-10}	-530.79	6.31×10^{-8}	-767.02
10Al10Y	1.56×10^{-3}	-87.20	1.72×10^{-8}	-581.67	1.10×10^{-3}	-79.87	1.30×10^{-9}	-545.26	4.76×10^{-8}	-763.06
10Al0.5Y	1.86×10^{-3}	-90.92	5.66×10^{-9}	-566.02	-	-	-	-	-	-

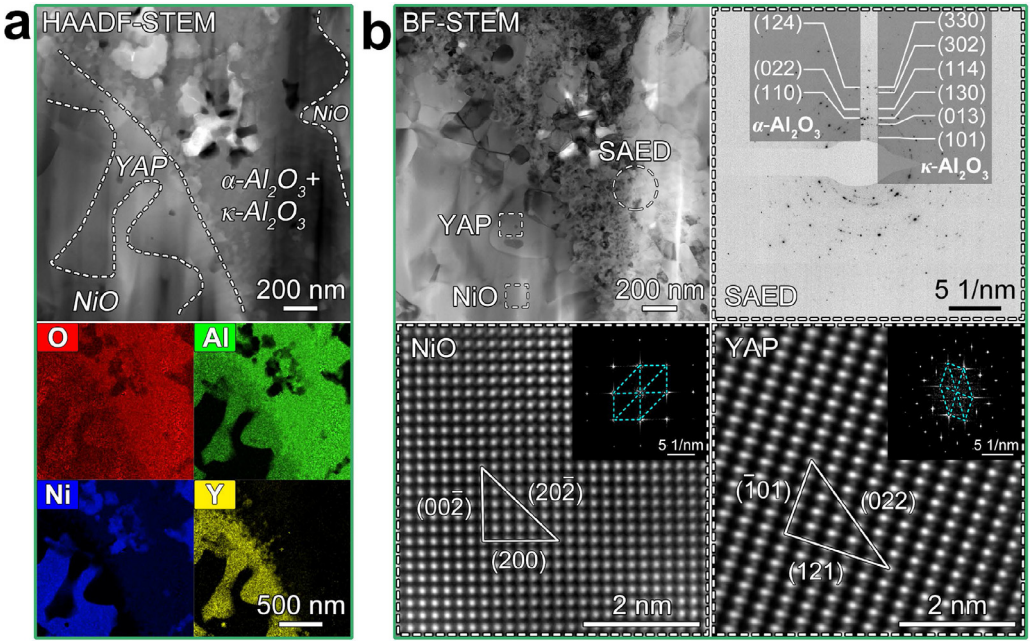

Fig. 9. Elemental distribution and oxidation species determinations via TEM performed on the 1000°C-oxidized 10Al0.5Y: (a) HAADF-STEM image and corresponding drift-corrected STEM-EDS mapping result showing the inner layer structure and elemental distribution after 200-hour exposure. (b) BF-STEM image and corresponding SAED pattern, and IFFT images of the indicated regions showing Al_2O_3 oxides along GBs, and the existence of NiO and YAP oxides.

dation at 800°C/1000°C, *i.e.*, outer NiO scale, and the inner mixed oxides/phases containing mainly YAM/YAP, Al_2O_3, and Ni-O interdiffusion zone. In the early stage, O^{2-} enters the substrate along the fast diffusion channels and reacts with high-activity Y and Al to form internal oxides [58,59]. However, due to the limited content of Al and Y in the alloys, a large number of regions containing low oxygen affinity Ni interpenetrate between these internal oxides, which hinders the formation of continuous oxide scale. With the increase of oxidation time, Ni^{+} accumulates on the outer surface and reacts with O^{2-} to form NiO scale, which further hinders the inward transport of O^{2-} and thusly lowers oxidation rate (Fig. 3 and 4). Huge difference between the three high-Y-content alloys is that the morphology of the inner layer strongly depends on the original microstructure due to the distribution and size of Ni_5Y phase containing high-activity Y and Al. In addition, the continuous oxide film is generally formed along PBs due to the more favorable transport condition.

According to the results, mixed inner phases containing YAM/YAP (depending on the oxidation temperature), κ-Al_2O_3/α-Al_2O_3, and γ-Ni form within the original-Ni_5Y region, while only Ni-O interdiffusion zone remains within the original-γ-Ni region. Typically, 22Al10Y has almost complete lamellar structure, composed of NiAl and Ni_5Y lamellae, which provide numerous PBs and facilitate the fast-inward flux of O^{2-} in early stage. However, derived from the dense lamellae and plenty of high-activity Al and Y around, further inward diffusion of O^{2-} could be probably inhibited by locally formed Y-rich and Al-rich or (Y, Al)-rich oxides. As revealed in Fig. 5, oxides (with dark contrast) predominately present along PBs. Due to the observed depletion of Al within original-NiAl phase after oxidation (Fig. 6a), the formation of oxides along PBs (mainly Al-O, Fig. 3 and S7a) could be reasonably ascribed to the transport of Al within NiAl toward PBs and reacting with O^{2-}.

Moreover, Y-rich and Al-rich or (Y, Al)-rich oxides are observed inside original-Ni_5Y phase (Fig. 3 and 6c). A large number of fine oxide interfaces also facilitate transverse diffusion of O^{2-} under the attraction of high-activity Al and Y. These formed oxides further weaken the possibility of oxygen's inward diffusion. After the oxidation of Al and Y, the remaining Ni would partly react with oxygen (becoming outer NiO layer), and partly become island Ni-O interdiffusion particles (denoted as γ-Ni) within original-Ni_5Y phase. Accordingly, the whole oxidation process can be simply summarized, as schematically shown in Fig. 10. Similarly, the oxidation processes of 10Al10Y and 10Al3Y can be described as same as 22Al10Y, since the phases within the three alloys are quite similar, only distinguished in size. According to the results of thickness, 10Al3Y with smaller Ni_5Y-phase region (contained in eutectic microstructure) exhibits slower oxidation rate than 10Al10Y with larger one (proeutectic phase). It means that coarse and isolated Ni_5Y particles may possess poorer oxidation resistance than mixed microstructures, *e.g.*, eutectic regions containing Ni_5Y and γ-Ni (Fig. 3).

4.3. Oxidation mechanism corresponding to the formation of Al_2O_3

Above experimental results have indicated major changes of the oxidation rate of 22Al10Y and 10Al0.5Y from 800°C to 1000°C. Except for the benefits from Y-related microstructures, the high Al content also deserves detailed discussion, because of the protective effect provided by Al_2O_3 oxides. According to the classical oxidation theory, the formation of Al_2O_3 can be qualitatively described. Considering the situation of Al_2O_3 oxides have a chance to convert to external scale, it would bring most desirable oxidation resistance. This process needs an atomic concentration condition, which has been concluded by Wagner, as following [38]:

$$N^{0}_{Al(min)} = \left(\frac{\pi g^{*} N^{\gamma}_{O} D^{\gamma}_{O} V^{\gamma}_{m}}{2 b D^{\gamma}_{Al} V^{Al_2O_3}_{m}} \right)^{1/2} \quad (7)$$

Where $N^{0}_{Al(min)}$ is the minimum concentration (atomic fraction) of Al in the γ-Ni matrix to originally develop an external Al_2O_3 scale; g^{*} is a critical volume fraction of the oxides within the inner

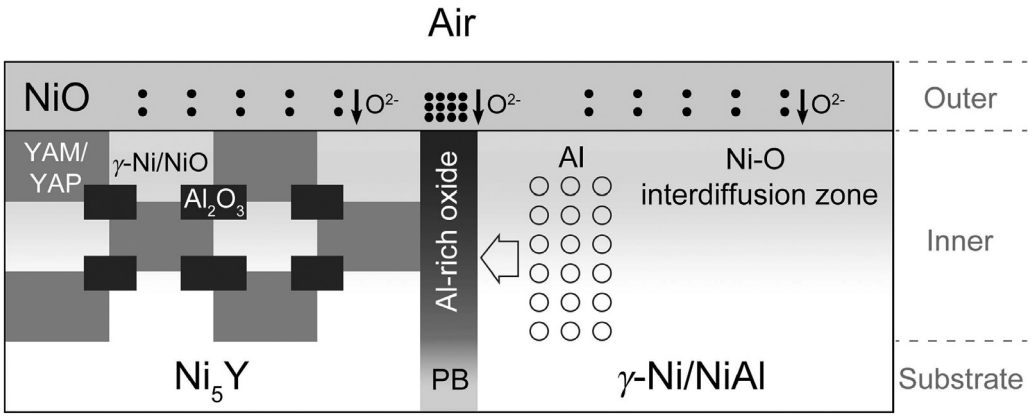

Fig. 10. Schematic illustration indicating the potential oxidation mechanism from the aspect of microstructural features.

layer, and is usually taken as 0.3 [50,60]; N_O^{γ} is solubility of oxygen in the γ-Ni matrix; D_O^{γ} is the diffusion coefficient of oxygen in the γ-Ni matrix; $N_O^{\gamma}D_O^{\gamma}$ is the oxygen permeability in γ-Ni; V_m^{γ} and $V_m^{Al_2O_3}$ is the molar volume of the γ-Ni and Al_2O_3, respectively; b is the coefficient of the oxide in MO_b type, *e.g.*, $AlO_{3/2}$; D_{Al}^{γ} is diffusion coefficient of Al in γ-Ni.

Even through the calculation of $N_{Al(min)}^0$ faces some difficulties, it is still of great significance to estimate reasonable values. The most important procedure is to determine the unknown value of $N_O^{\gamma}D_O^{\gamma}$ and D_{Al}^{γ}. According to the oxidation kinetics, the inner layer thickness can be quantitatively derived by using Fick's first law and mass conservation [40]:

$$X_t = \left(\frac{2N_O^{\gamma}D_O^{\gamma}}{bN_{Al}^0}t\right)^{1/2} \tag{8}$$

Where X_t is the inner layer thickness after oxidation for time t; N_{Al}^0 is the initial concentration of Al in the γ-Ni matrix. Eq. (8) can also be represented using a classical parabolic type by introducing a parabolic rate constant, k_p:

$$X_t = k_p^{1/2}t^{1/2} \text{or } X_t^2 = k_p t \tag{9}$$

The dependence of X_t with t can be measured by using the experimental results. Then, the value of k_p can be estimated by fitting the experimental data concerning X_t^2~ t. So, the value of $N_O^{\gamma}D_O^{\gamma}$ can be reasonably estimated. D_{Al}^{γ} can be retrieved from DICTRA (Fig. 11a). Due to the different and complicated microstructures, the actual value of g* of the alloys described in the present investigation still remains unknown. However, it is possible to set some numerical values for g* according to the experimental results, *e.g.*, 0.1~0.7, which will lead to a reasonable value of $N_{Al(min)}^0$ not exceeding unity. Finally, a series of curves concerning the relationship between $[N_{Al(min)}^0]^2$ and g* can be established, as shown in Fig. 11b.

According to Fig. 11b, 22Al10Y, with a high Al content, possesses a rather low value of $[N_{Al(min)}^0]^2$ in the case of 800°C, compared to 10Al0.5Y and 10Al3Y. This demonstrates that the very low oxidation rate of 22Al10Y at 800°C (Fig. 4) could be partly ascribed to its high possibility to realizing the transition of Al_2O_3 to an external scale or the growth of massive Al_2O_3 oxides at PBs. While the temperature increases to 1000°C, the value, $[N_{Al(min)}^0]^2$, of 22Al10Y increases slightly. The increased inner layer of 22Al10Y indicates that the advantages depicted in the case of 800°C are not enough to prevent the alloy from further oxidation at 1000°C. This could be ascribed to the high Y content and massive growth of Y-Al-O oxides, which would consume the around Al, thusly leading to

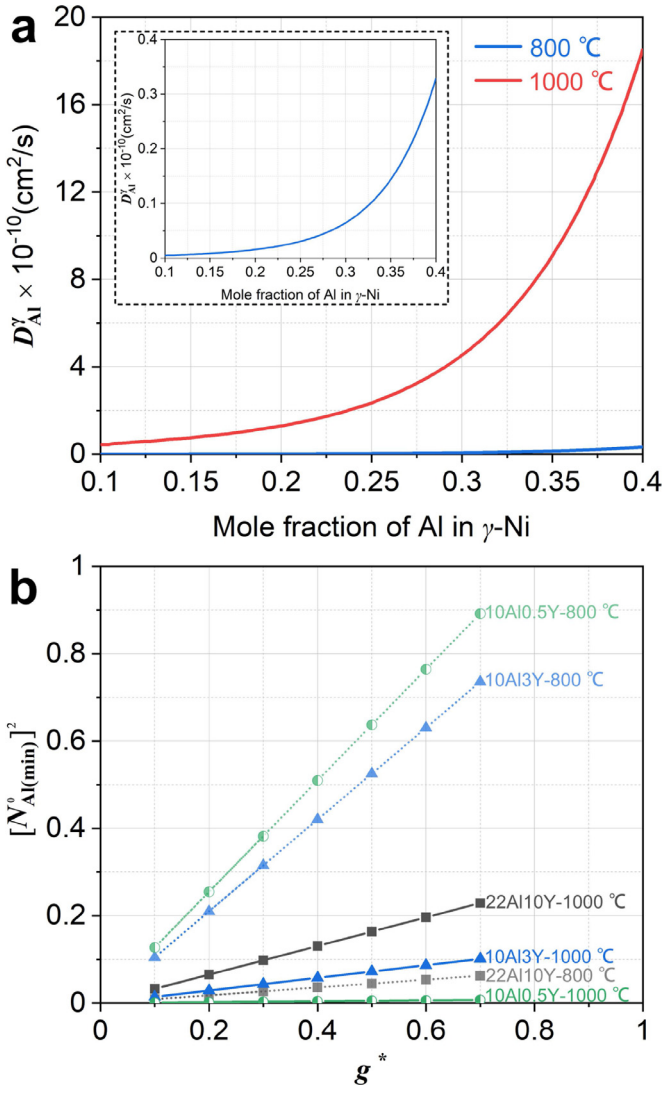

Fig. 11. (a) Calculated diffusion coefficient of Al in γ-Ni. (b) Calculated minimum concentration (square value) of Al in γ-Ni to develop exclusive Al_2O_3 scale.

a lower ability for the growth of Al_2O_3. Then, the significantly decreasing of $[N_{Al(min)}^0]^2$ of 10Al0.5Y and 10Al3Y from 800°C to 1000°C deserves special discussion. Here we take 10Al0.5Y as an example. A very low content of Y does not bring obvious advantage

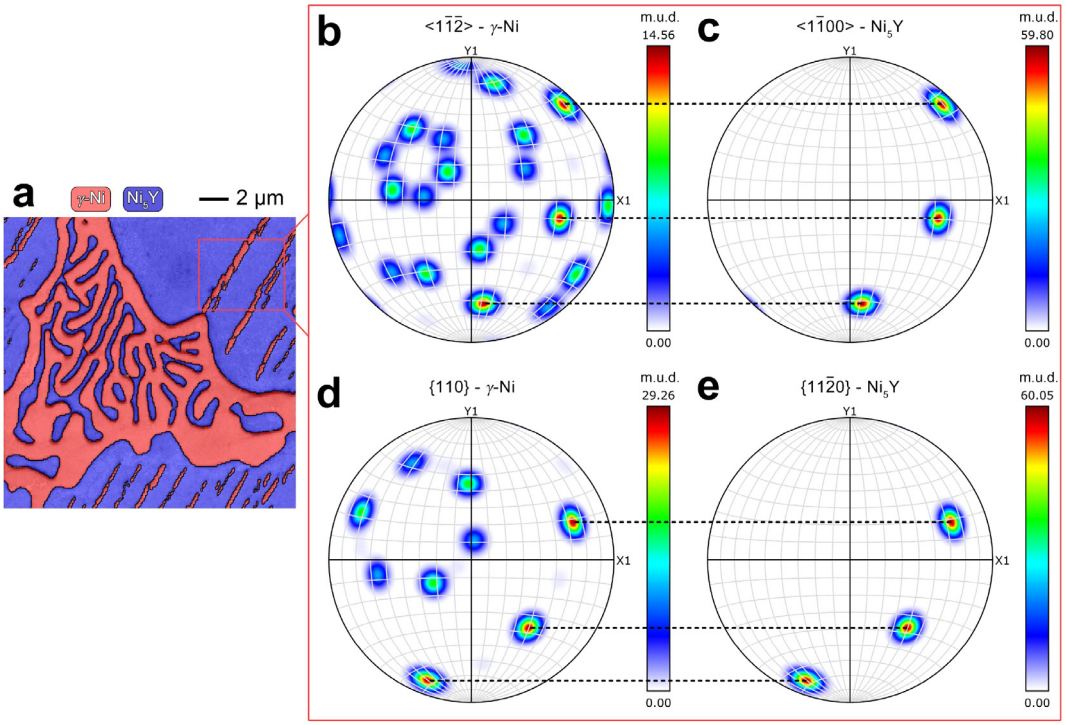

Fig. 12. (a) EBSD phase map of a specific area observed in 10Al10Y alloy after 200-hour exposure at 800°C showing the precipitation of secondary γ-Ni strips within parent Ni_5Y crystal. (b)-(e) Pole figure (PF) analysis of the region indicated in (a) showing the perfect orientation between the parent Ni_5Y and secondary γ-Ni.

to the matrix during resisting oxidation at 800°C, but conversely provides fast diffusion channel (Y-related phases at GBs) for oxygen. Simultaneously, the solution Al provides little ability for the growth of Al_2O_3 at the relatively low D^{γ}_{Al} (6.19E-13 cm^2/s at 800°C verse 5.26E-11 cm^2/s at 1000°C). So, the significantly increased D^{γ}_{Al} at 1000°C consequently lowers the value of $[N^0_{Al(min)}]^2$.

According to Fig. S6 and 9, massive Al_2O_3 oxides have occupied the front of the inner layer and PBs or GBs in 10Al0.5Y, indicating a better ability for inhibiting the inward diffusion of oxygen. Particularly, the growth of Al_2O_3 and YAP oxides along GBs or PBs (Fig. 9) inhibit the inward diffusion of oxygen anion and outward diffusion of metal cations [35,61]. Moreover, the continuous Al_2O_3 along the front of the inner layer (Fig. S6) further inhibits the development of oxidation toward the inner matrix, thusly resulting in the internally nucleation and growth of NiO oxides (Fig. 9) under the condition that Al and Y has been consumed. Finally, the overall effects make the alloy 10Al0.5Y possess a desirable oxidation resistance at 1000°C compared to the other three alloys. Note that, the calculation of $[N^0_{Al(min)}]^2$ did not involve 10Al10Y, because of its high fraction of Ni_5Y and limited fraction of γ-Ni. Its oxidation mechanism will be discussed in the following section.

4.4. Precipitation-induced oxidation

It should be noted that even if Ni_5Y phase is not pre-oxidized, it is possible to form specific micro morphology after long-term thermal exposure to facilitate the transport of O^{2-}, *e.g.*, strip-shaped γ-Ni phase is obviously formed within primary Ni_5Y particle of 10Al10Y (Fig. 12). These newly formed γ-Ni strips are arranged in parallel within the parent Ni_5Y crystal with an perfect orientation relationship as follow: $<1\bar{1}2>_{\gamma-Ni} \| <1\bar{1}00>_{Ni_5Y}$ & $\{110\}_{\gamma-Ni} \| \{11\bar{2}0\}_{Ni_5Y}$. The newly formed PBs lead to simultaneous oxidation of eutectic region and primary phase, which makes the thickness of inner layer of 10Al10Y much higher than that of the other two alloys.

4.5. κ-Al_2O_3 and α-Al_2O_3

The κ-Al_2O_3 observed in TEM study is not predicted in the modified diagram because the adopted thermodynamic database does not contain such metastable phase. Nevertheless, by analyzing the oxidation behavior of Ni_5Y phase, κ-Al_2O_3 may probably exist, due to the very early reaction between O and Al/Y forming Al_2O_3/Y_2O_3, and finally forming YAP and YAM, as exhibited in Eq. (5) and (6). Among them, YAP and Al_2O_3 may be transformed into each other. Generally, the lattice potential of the position occupied by Y^{3+} in YAP is higher than that of Al^{3+}, which indicates that Y^{3+} position is easier to be introduced into cation vacancy, or the diffusion capability of Y^{3+} is stronger than that of Al^{3+} commonly [62]. Therefore, Y^{3+} can further react with newly introduced O^{2-} to form Y_2O_3 or be combined with residual Al^{3+} to form YAM. κ-Al_2O_3 was reported stable when temperature below ~927°C [54]. This means that the transition from κ-Al_2O_3 to α-Al_2O_3 is unlikely to extensively occur at 800°C, but it is possible to occur at 1000°C. This is consistent with our findings in the present study.

5. Conclusions

In conclusion, the isothermal oxidation behavior of Ni-Al-Y ternary alloys at 800°C/1000°C for 1~200 h has been investigated in detail through SEM, XRD, EBSD, TKD, and TEM. Yttrium-related microstructures, such as precipitation of γ-Ni stripes within Ni_5Y crystal, eutectic phases containing Ni_5Y, and nanoscale lamellae, were found have strong effect on the oxide evolution and oxidation layer development. These effects are also influenced strongly by protective component, Al. The results and discussion lead to the following conclusions concerning the oxide evolution over time.

(1) Ni_5Y and γ-Ni phases are beneficial to the formation of inner layer containing mixed YAM/YAP and κ-Al_2O_3/α-Al_2O_3 (depending on oxidation temperature), and NiO outer scale or Ni-O interdiffusion zone, respectively.

(2) 22Al10Y alloy with lamellar structure exhibits significant resistance to inner oxidation at 800°C due to its nanoscale lamellae and high Al content (promoting the growth of Al_2O_3). In 10Al3Y alloy, the transport of O^{2-} along the eutectic PBs dominates the development of inner oxidation. The minor-Y-addition alloy 10Al0.5Y exhibits better internal oxidation resistance at 1000°C than that of 800°C, resulting from the mixed Al_2O_3 and YAP oxides along GBs or PBs and front of inner layers.
(3) A precipitation-induced oxidation behavior has been revealed in 10Al10Y alloy by examining the supersaturated Ni_5Y crystal (precipitating secondary γ-Ni strips), which promoted the inner oxidation layer development.
(4) From the aspect of thermodynamics, a type of modified diagram retrieved from ternary isothermal section is effective to predicted the oxide evolution, compared with experimental results.

Data availability

The datasets generated during and/or analyzed during the current study are available from the corresponding author upon request.

Author contributions

Y.W., Y.L., M.K., and J.W. conceived the project and designed the experiments. Y.W. performed all experiments. Y.L. and Y.X. assisted Y.W. on EBSD and STEM. B.S. discussed the results. Y.W. and Y.L. analyzed the data and wrote the paper assisted by M.K. and J.W. All authors reviewed and approved the manuscript.

Declaration of Competing Interest

The authors declare that they have no known competing financial interests or personal relationships that could have appeared to influence the work reported in this paper.

Acknowledgements

This work was financially supported by the National Natural Science Foundation of China (No. 51971142, 52031012), National Science and Technology Major Project of China (No. 2017-VI-0013-0085), Aeronautical Science Foundation of China (No. 2018ZE57012), and Startup Fund for Youngman Research at SJTU (No. 18×100040027). B.S. would like to acknowledge the technical support from Instrumental Analysis Center, Shanghai Jiao Tong University. Y.W. would like to acknowledge the software support from Oxford Instruments NanoAnalysis.

Supplementary materials

Supplementary material associated with this article can be found, in the online version, at doi:10.1016/j.actamat.2021.116879.

References

[1] R.C. Reed, The Superalloys: Fundamentals and Applications, Cambridge University Press, 2006.
[2] T.M. Pollock, Alloy design for aircraft engines, Nat. Mater. 15 (8) (2016) 809–815.
[3] R. Viswanathan, K. Coleman, U. Rao, Materials for ultra-supercritical coal-fired power plant boilers, Int. J. Pres. Ves. Pip. 83 (11-12) (2006) 778–783.
[4] D. Tytko, P.-P. Choi, J. Klöwer, A. Kostka, G. Inden, D. Raabe, Microstructural evolution of a Ni-based superalloy (617B) at 700°C studied by electron microscopy and atom probe tomography, Acta Mater. 60 (4) (2012) 1731–1740.
[5] T.M. Smith, B.D. Esser, N. Antolin, A. Carlsson, R.E. Williams, A. Wessman, T. Hanlon, H.L. Fraser, W. Windl, D.W. McComb, M.J. Mills, Phase transformation strengthening of high-temperature superalloys, Nat. Commun. 7 (2016) 13434.
[6] A. Sato, Y.L. Chiu, R.C. Reed, Oxidation of nickel-based single-crystal superalloys for industrial gas turbine applications, Acta Mater. 59 (1) (2011) 225–240.
[7] Z. Zhang, Z. Yang, S. Lu, A. Harte, R. Morana, M. Preuss, Strain localisation and failure at twin-boundary complexions in nickel-based superalloys, Nat. Commun. 11 (1) (2020) 4890.
[8] H.S. Kitaguchi, H.Y. Li, H.E. Evans, R.G. Ding, I.P. Jones, G. Baxter, P. Bowen, Oxidation ahead of a crack tip in an advanced Ni-based superalloy, Acta Mater. 61 (6) (2013) 1968–1981.
[9] H.T. Mallikarjuna, W.F. Caley, N.L. Richards, The dependence of oxidation resistance on gamma prime intermetallic size for superalloy IN738LC, Corros. Sci. 147 (2019) 394–405.
[10] Y. Liu, Y. Wu, J. Wang, Y. Ning, Oxidation behavior and microstructure degeneration of cast Ni-based superalloy M951 at 900 °C, Appl. Surf. Sci. 479 (2019) 709–719.
[11] D.J. Young, High Temperature Oxidation and Corrosion of Metals, Elsevier Science, 2008.
[12] B. Zhang, X. Lu, D. Liu, C. Tao, Influence of recrystallization on high-temperature stress rupture property and fracture behavior of single crystal superalloy, Mater. Sci. Eng. A 551 (2012) 149–153.
[13] T.M. Pollock, A.S. Argon, Creep resistance of CMSX-3 nickel base superalloy single crystals, Acta Metall. Mater. 40 (1) (1992) 1–30.
[14] M. Bensch, J. Preußner, R. Hüttner, G. Obigodi, S. Virtanen, J. Gabel, U. Glatzel, Modelling and analysis of the oxidation influence on creep behaviour of thin-walled structures of the single-crystal nickel-base superalloy René N5 at 980°C, Acta Mater. 58 (5) (2010) 1607–1617.
[15] J. Tong, S. Dalby, J. Byrne, M.B. Henderson, M.C. Hardy, Creep, fatigue and oxidation in crack growth in advanced nickel base superalloys, Int. J. Fatigue 23 (10) (2001) 897–902.
[16] A.G. Evans, M.Y. He, A. Suzuki, M. Gigliotti, B. Hazel, T.M. Pollock, A mechanism governing oxidation-assisted low-cycle fatigue of superalloys, Acta Mater. 57 (10) (2009) 2969–2983.
[17] M.Y. He, A.G. Evans, A model for oxidation-assisted low cycle fatigue of superalloys, Acta Mater. 58 (2) (2010) 583–591.
[18] X.-X. Yu, M.A. Taylor, J.H. Perepezko, L.D. Marks, Competition between thermodynamics, kinetics and growth mode in the early-stage oxidation of an equimolar CoCrFeNi alloy, Acta Mater. 196 (2020) 651–659.
[19] K. Fueki, J.B. Wagner, Studies of the oxidation of nickel in the temperature range of 900° to 1400°C, J. Electrochem. Soc. 112 (4) (1965) 384–388.
[20] A.D. Dalvi, D.E. Coates, A review of the diffusion path concept and its application to the high-temperature oxidation of binary alloys, Oxid. Met. 5 (2) (1972) 113–135.
[21] A. Atkinson, Transport processes during the growth of oxide films at elevated temperature, Rev. Mod. Phys. 57 (2) (1985) 437–470.
[22] B. Pieraggi, Calculations of parabolic reaction rate constants, Oxid. Met. 27 (3-4) (1987) 177–185.
[23] T.J. Nijdam, L.P.H. Jeurgens, W.G. Sloof, Modelling the thermal oxidation of ternary alloys—compositional changes in the alloy and the development of oxide phases, Acta Mater. 51 (18) (2003) 5295–5307.
[24] T.J. Nijdam, W.G. Sloof, Effect of reactive element oxide inclusions on the growth kinetics of protective oxide scales, Acta Mater. 55 (17) (2007) 5980–5987.
[25] M. Bensch, A. Sato, N. Warnken, E. Affeldt, R.C. Reed, U. Glatzel, Modelling of high temperature oxidation of alumina-forming single-crystal nickel-base superalloys, Acta Mater. 60 (15) (2012) 5468–5480.
[26] B.A. Pint, J.R. Martin, L.W. Hobbs, The oxidation mechanism of θ-Al_2O_3 scales, Solid State Ion. 78 (1-2) (1995) 99–107.
[27] P. Castello, F.H. Stott, F. Gesmundo, Yttrium-promoted selective oxidation of aluminium in the oxidation at 1100°C of an eutectic Ni-Al-Cr_3C_2 alloy, Corros. Sci. 41 (5) (1999) 901–918.
[28] X.L. Li, S.M. He, X.T. Zhou, Y. Zou, Z.J. Li, A.G. Li, X.H. Yu, Effects of rare earth yttrium on microstructure and properties of Ni-16Mo-7Cr-4Fe nickel-based superalloy, Mater. Charact. 95 (2014) 171–179.
[29] K. Kawagishi, H. Harada, A. Sato, A. Sato, T. Kobayashi, The oxidation properties of fourth generation single-crystal nickel-based superalloys, JOM 58 (1) (2006) 43–46.
[30] W. Wang, P. Yu, F. Wang, S. Zhu, The effect of yttrium addition on the isothermal oxidation behavior of sputtered K38 nanocrystalline coating at 1273 K in air, Surf. Coat. Tech. 201 (16-17) (2007) 7425–7431.
[31] K.-D. Xu, Z.-M. Ren, C.-J. Li, Progress in application of rare metals in superalloys, Rare Metals 33 (2) (2014) 111–126.
[32] J.D. Kuenzly, D.L. Douglass, The oxidation mechanism of Ni_3Al containing yttrium, Oxid. Met. 8 (3) (1974) 139–178.
[33] T. Xu, S. Faulhaber, C. Mercer, M. Maloney, A. Evans, Observations and analyses of failure mechanisms in thermal barrier systems with two phase bond coats based on NiCoCrAlY, Acta Mater. 52 (6) (2004) 1439–1450.
[34] Y. Chen, X. Zhao, P. Xiao, Effect of microstructure on early oxidation of MCrAlY coatings, Acta Mater. 159 (2018) 150–162.
[35] J. Lu, Y. Chen, H. Zhang, C. Zhao, X. Zhao, F. Guo, P. Xiao, Superior oxidation and spallation resistant NiCoCrAlY bond coat via homogenizing the yttrium distribution, Corros. Sci. 159 (2019) 108145.
[36] D. Texier, E. Copin, A. Flores, J. Lee, M. Terner, H.U. Hong, P. Lours, High temperature oxidation of NiCrAlY coated alloy 625 manufactured by selective laser melting, Surf. Coat. Tech. 398 (2020) 126041.
[37] A. Gil, D. Naumenko, R. Vassen, J. Toscano, M. Subanovic, L. Singheiser, W.J. Quadakkers, Y-rich oxide distribution in plasma sprayed MCrAlY-coatings studied by SEM with a cathodoluminescence detector and Raman spectroscopy, Surf. Coat. Tech. 204 (4) (2009) 531–538.

[38] C. Wagner, Reaktionstypen bei der Oxydation von Legierungen, Zeitschrift für Elektrochemie, Berichte der Bunsengesellschaft für physikalische Chemie 63 (7) (1959) 772–782.
[39] E. Schumann, M. Rühle, Microstructural observations on the oxidation of γ'-Ni_3Al at high oxygen partial pressure, Acta Metall. Mater. 42 (4) (1994) 1481–1487.
[40] N. Birks, G.H. Meier, F.S. Pettit, Introduction to the High Temperature Oxidation of Metals, Cambridge University Press, 2006.
[41] W.J. Golumbfskie, S.N. Prins, T.J. Eden, Z.K. Liu, Predictions of the Al-rich region of the Al-Co-Ni-Y system based upon first-principles and experimental data, Calphad 33 (1) (2009) 124–135.
[42] F. Bachmann, R. Hielscher, H. Schaeben, Texture analysis with MTEX - free and open source software toolbox, Solid State Phenom 160 (2010) 63–68.
[43] B. Beausir, J.-J. Fundenberger, Analysis Tools for Electron and X-ray Diffraction, ATEX - software, 2017 www.atex-software.eu.
[44] D.R. Gaskell, D.E. Laughlin, Introduction to the Thermodynamics of Materials, CRC Press, 2017 Sixth Edition.
[45] I. Barin, O. Knacke, O. Kubaschewski, Thermochemical Properties of Inorganic Substances, Springer, Berlin Heidelberg, 1973.
[46] I. Barin, O. Knacke, O. Kubaschewski, Thermochemical Properties of Inorganic Substances: Supplement, Springer, Berlin Heidelberg, 2013.
[47] Z.-K. Liu, Computational thermodynamics and its applications, Acta Mater. 200 (2020) 745–792.
[48] B. Sundman, B. Jansson, J.-O. Andersson, The Thermo-Calc databank system, Calphad 9 (2) (1985) 153–190.
[49] J.O. Andersson, T. Helander, L. Höglund, P. Shi, B. Sundman, Thermo-Calc & DICTRA, computational tools for materials science, Calphad 26 (2) (2002) 273–312.
[50] R.A. Rapp, Kinetics, microstructures and mechanism of internal oxidation - its effect and prevention in high temperature alloy oxidation, Corrosion 21 (12) (1965) 382–401.
[51] D.L. Douglass, A critique of internal oxidation in alloys during the post-wagner era, Oxid. Met. 44 (1-2) (1995) 81–111.
[52] K. Chen, L. Zhang, Z. Shen, Understanding the surface oxide evolution of T91 ferritic-martensitic steel in supercritical water through advanced characterization, Acta Mater. 194 (2020) 156–167.
[53] B. Ollivier, R. Retoux, P. Lacorre, D. Massiot, G. Férey, Crystal structure of κ-alumina: an X-ray powder diffraction, TEM and NMR study, J. Mater. Chem. 7 (6) (1997) 1049–1056.
[54] Y. Yourdshahyan, C. Ruberto, M. Halvarsson, L. Bengtsson, V. Langer, B.I. Lundqvist, S. Ruppi, U. Rolander, Theoretical structure determination of a complex material: κ-Al_2O_3, J. Am. Ceram. Soc. 82 (6) (1999) 1365–1380.
[55] C. Wolverton, K.C. Hass, Phase stability and structure of spinel-based transition aluminas, Phys. Rev. B 63 (2) (2000) 024102.
[56] Z. Lodziana, N.Y. Topsoe, J.K. Norskov, A negative surface energy for alumina, Nat. Mater. 3 (5) (2004) 289–293.
[57] A. Stierle, F. Renner, R. Streitel, H. Dosch, W. Drube, B.C. Cowie, X-ray diffraction study of the ultrathin Al_2O_3 layer on NiAl(110), Science 303 (5664) (2004) 1652–1656.
[58] R. Diehl, G. Brandt, Crystal structure refinement of $YAlO_3$, a promising laser material, Mater. Res. Bull. 10 (2) (1975) 85–90.
[59] T.J. Nijdam, W.G. Sloof, Effect of Y distribution on the oxidation kinetics of NiCoCrAlY bond coat alloys, Oxid. Met. 69 (1-2) (2007) 1–12.
[60] Z.G. Zhang, F. Gesmundo, P.Y. Hou, Y. Niu, Criteria for the formation of protective Al_2O_3 scales on Fe-Al and Fe-Cr-Al alloys, Corros. Sci. 48 (3) (2006) 741–765.
[61] P.A. van Manen, E.W.A. Young, D. Schalkoord, C.J. van Der Wekken, J.H.W. de Wit, The influence of Y on the structure and growth mechanism of alumina scales, Surf. Interface Anal. 12 (7) (1988) 391–396.
[62] T. Maruyama, K. Kawamura, A. Saiki, K. Nagata, Thermodynamics and diffusivity of yttrium in yttrium chromite ($YCrO_3$), Key Eng. Mater. 111-112 (1995) 303–320.